FULL PAPER

Flexible Photodetectors

ADVANCED
OPTICAL
MATERIALS

www.advopticalmat.d

All-Sprayed-Processable, Large-Area, and Flexible Perovskite/MXene-Based Photodetector Arrays for Photocommunication

Wen Deng, Haichao Huang, Huaimin Jin, Wen Li, Xiang Chu, Da Xiong, Wei Yan, Fengjun Chun, Meilin Xie, Chao Luo, Long Jin, Chuanqi Liu, Haitao Zhang, Weili Deng, and Weiqing Yang*

Flexible photodetectors (PDs) are attracting more attention due to their promising applications in wearable optoelectronic devices, bendable imaging sensors, and implantable optoelectronics. For the easy-processable technology of massively fabricating PDs, instead of the expensive and complex high-vacuum technique, the well-matched work function of their active materials is essential. Herein, all-sprayed-processable and large-area PDs are demonstrated on common paper based on two-dimensional (2D) $CsPbBr_3$ nanosheets and conductive $Ti_3C_2T_x$ (MXene). Ascribed to the superior conductivity of MXene, high crystallinity of 2D $CsPbBr_3$, and their well-matched work function, the as-prepared PDs exhibit an outstanding on/off current ratio up to 2.3×10^3 and a remarkable photoresponse as fast as 18 ms. Specifically, the detectivity (D^*) of 6.4×10^8 Jones and responsivity (R) of 44.9 mA W^{-1} under a bias of 10 V are achieved. Besides, after bending 1500 cycles, the as-prepared PDs can still maintain the excellent flexibility and stability. Based on this, a superior-quality and large-area 1665 pixel sensor in 72 cm^2 ($\approx$24 units cm^{-2}) is developed, and it can clearly transmit the image of "0" to realize the photocommunication function. This work provides a low-cost method of massively producing the flexible large-area PDs for wearable optoelectronic devices and expanded photocommunication.

1. Introduction

Photodetectors (PDs) for photoelectric signal conversion are attracting an increasing attention in scientific research and industrial realms due to its wide applications, such as optical communications, environmental monitoring, and biological detection.[1] Currently, the widely used active materials of PDs are dominated by crystalline-Si and III–V alloys for the detection of ultraviolet (UV) to near-infrared spectra.[2] However, the above PDs are usually assembled on rigid substrates, which seriously limits its wider applications in the field of flexible optoelectronics devices, such as wearable optoelectronic devices, bendable imaging sensors, and implantable optoelectronics devices.[3] Contrary to rigid PDs, flexible PDs can essentially meet the stretchable and bendable demands for intelligentized applications. Both high optoelectronic performance and excellent mechanical flexibility should be simultaneously integrated in one device, which is still a great

challenge for the active materials, electrodes, substrates and fabrication technique to date.[4] Therefore, in order to obtain the flexible PDs with the above two advantages, the as-prepared devices must meet the following requirements: i) the sufficiently thin active materials for effectively releasing stress together with the relatively low degradation of photoelectrical properties when bending; ii) the well-matched work function between the optimal electrode materials and active materials in order to effectively transport photogenerated electron–hole pairs; and iii) the low-cost, large-area, and easy-processable fabrication techniques for promisingly replacing the expensive and complex high-vacuum process technology.[5]

Recently, all-inorganic perovskites ($CsPbX_3$) are hopeful to be widely used in optoelectronics devices due to the unique photoelectric properties, such as large absorption coefficient (2×10^5 cm^{-1}), high charge carrier mobility (1000 cm^2 V^{-1}), long electron–hole diffusion, and tunable bandgap.[6] Particularly, compared to traditional crystalline-Si, all-inorganic perovskites can be processed by more economical solution-processing

W. Deng, H. C. Huang, H. M. Jin, W. Li, X. Chu, D. Xiong, F. J. Chun, M. L. Xie, C. Luo, L. Jin, Dr. H. T. Zhang, Dr. W. L. Deng, Prof. W. Q. Yang
Key Laboratory of Advanced Technologies of Materials
(Ministry of Education)
School of Materials Science and Engineering
Southwest Jiaotong University
Chengdu 610031, China
E-mail: wqyang@swjtu.edu.cn
Prof. W. Yan
State Key Laboratory of Optical Technologies for Microfabrication
Institute of Optics and Electronics
Chinese Academy of Sciences
Chengdu 610209, China
C. Q. Liu
College of Optoelectronic Technology
Chengdu University of Information Technology
Chengdu 610225, China

The ORCID identification number(s) for the author(s) of this article can be found under https://doi.org/10.1002/adom.201801521.

technique, strongly implying its huge potential in low-cost, large-area, and flexible PDs.[7] Usually, for the flexible PDs, the compact perovskite thin film is a key to obtain the high optoelectronic performance, which can effectively reduce the occurrence of leakage current.[8] However, owing to the low solubility and fast evaporation of perovskite precursors, the one-step processed perovskite films easily exhibit poor compactness and uncontrollable thickness after annealing treatment, which will badly decrease the conductivity of the films.[9] Fortunately, 2D perovskite nanosheets not only can effectively overlap with each other to form a dense optical absorption layer but also have highly crystalline nanostructure, thus essentially improving the electrical conductivity of the films.[10] Besides, 2D perovskite nanosheets have two natural advantages for flexible PDs. On one hand, the surface uniformity and high crystallization quality of the ultrathin nanosheet structure have good compatibility with flexible substrate, which makes them a rational choice for the preparation of flexible electronic devices. On the other hand, compared with their bulk materials, the low-dimensional chip structure has stronger spatial confinement effect and longer carrier lifetime, so its corresponding photodetectors are more easily to obtain higher photoresponse.[11] Therefore, there is no doubt that 2D perovskite nanosheets have a potential application in high performance, ultrathin and flexible PDs.

As an another integral part of the flexible PDs, the widely used electrodes are often Au, Ag, indium tin oxide (ITO) and others, due to their excellent conductivity and toughness.[1c,12] However, their costly and complex high-vacuum preparation process greatly hinders their large-area fabrication and then the wider commercial applications for flexible PDs. Recently, the solution-processable 2D $Ti_3C_2T_x$ (MXene), with exceptionally metallic conductivity, adjustable work function, and good transmittance, can overlap into fish-scale-like conductive films for flexible electronic devices.[13] By controlling transition metal element (such as Al, Ti, Zr, Hf, V, Nb, Ta, Cr, and Sc) of ternary layered carbides and nitride (MAX) phase, the work function of etched MXene can be accurately regulated in a large range of 2.14–5.65 eV.[14] Besides, the enriched surface functional groups (−OH, −O, and −F) around the lamellar MXene can remarkably improve its hydrophilia and dispersion in aqueous solution, intrinsically enlarging the massively low-cost processing method.[15]

In this work, we report the all-sprayed-processable, large-area, and flexible PDs arrays by combining 2D MXene with 2D $CsPbBr_3$ on common paper as the electrode and active materials, respectively. By the benefit of the well-matched work function between MXene and $CsPbBr_3$, the as-prepared PDs exhibit a high photo-to-dark current ratio of up to 2.3×10^3, coupled with the high response speed of 18 ms. Moreover, its bending tests demonstrated the excellent flexibility and stability of the devices. Importantly, a large-area 1665 pixel sensor arrays successfully achieve the digital "0" image for photocommunication. Therefore, this kind of all-sprayed-processable method will open up a way to massively fabricate large-area and flexible PDs arrays with high performance for wearable optoelectronic devices and photocommunication. Moreover, it can be potentially expanded to the other optoelectronic devices, such as thin film transistors, solar cells, and light-emitting diodes (LEDs).

2. Results and Discussion

Figure 1 clearly presents the schematics, detection mechanism, preparation process, and photographs of as-prepared flexible PDs. As shown Figure 1a, under the illumination of 450 nm light, the flexible large-area arrays PDs schematically transmitted a patterned digital "0" for realizing photocommunication function. Further, the corresponding results were simulated to clearly display the pattern of "0" by testing the photoelectric performance of these irradiated PDs (Figure 1b). This result is mainly ascribed to the newly
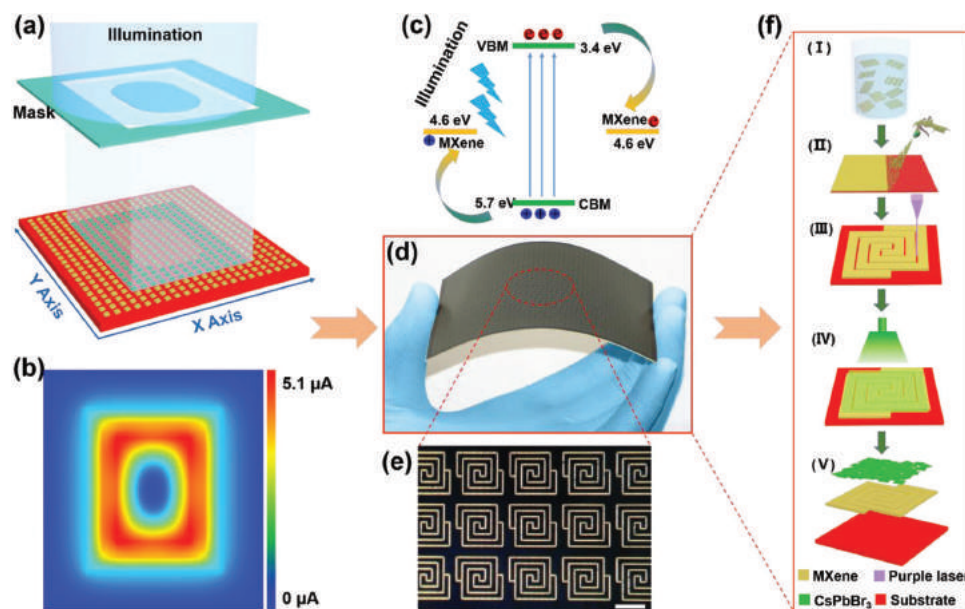

Figure 1. Schematic illustration of large-area array PDs fabrication. a) Schematic of a digital sensor based on large-area arrays 1665 pixel PDs. b) Analog digital display according to the detected data of lighting area. c) Energy level diagram of the semiconductor materials and MXene electrode in our devices. d) Exhibition of large-area arrays MXene electrode and e) corresponding microscopic pattern. The scale is 1 mm. f) The preparation process of the flexible PDs.

designed and well-matched energy level between the 2D CsPbBr$_3$ and MXene electrodes. In detail, the energy band alignment of the as-prepared devices clearly demonstrates the lower barrier (1.2 eV) of photogenerated electrons/holes from the conduction band minimum (CBM)/valence band maximum (VBM) of CsPbBr$_3$ to MXene electrodes (Figure 1c).[11] Figure 1d,e presents the photographs and its enlarged image of a superior quality and large-area workability 1665 pixel PDs array in 72 cm^2 (≈24 units cm^{-2}), respectively. Obviously, the PDs array owns the uniform surface and flexibility. Moreover, as demonstrated in Figure 1f, its preparation procedure can be divided in detail into three steps: i) the as-prepared MXene colloidal solution was spray-coated on a common paper to form the uniform and highly interconnected conductive thin film; ii) the elaborately selected cold working process technique was employed to carve the large-area arrays and coiled-shape MXene electrodes in order to avoid the destroyed structure of MXene; and iii) the as-prepared 2D CsPbBr$_3$ as the light absorbing materials of PDs also were spray-casted on the MXene electrode arrays to induce carriers. All the steps involved in this fabrication process were described in detail in the Experimental Section and Movie S1 in the Supporting Information.

For the deep insight into the microscopic features and crystal structure of MXene electrodes, its scanning electron microscope (SEM), transmission electron microscopy (TEM), energy-dispersive spectroscopy (EDS-mapping) images, and X-ray diffraction (XRD) patterns were systematically illustrated in **Figure 2**. As shown in Figure 2a, the SEM image clearly demonstrates the multilayered structure of as-prepared MXene. The TEM image (Figure 2b) of a single-layered MXene further demonstrates the flake structure with several micrometers. In addition, according to the EDS-mapping analysis (Figure 2c), Ti and C are the main elements, and O, F, and H occupy a smaller proportion at the same time, which can yield the evident conclusion that the Al atom layer was mostly removed from Ti$_3$AlC$_2$ phase (Figure 2c). Consequently, the abundant terminations (−OH, −O, and −F) introduced during the etching and ultrasonic exfoliation processes will introduce

the main driving forces for MXene flakes to assemble on other substrates including electrostatic forces, hydrogen bonding, and van der Waals forces.[16] Therefore, based on the above-mentioned unique capabilities of MXene, it is easy to spray coated on common paper.[17] And the thickness of MXene thin film can be well controlled by tuning the sprayed area and volume of MXene solution. Experimentally, 20 mL MXene solution was sprayed on a paper of 96 cm^2. As the SEM shown in Figure 2d and its inset, the as-sprayed MXene thin film presents a flat surface and its section thickness is about 7 μm. In addition, from its XRD patterns (Figure 2e), typical (002) plane at ≈7° evidently reveals successful delamination of 2D MXene flakes.[5b] And its c-lattice parameter is calculated as 27.6 Å, which is larger than the theoretical value (18.6 Å), once again implying the presence of surface functional groups (−OH, −O, and −F) surrounding the MXene flakes.[14b] In addition, the survey of ultraviolet photoelectron spectroscopy (UPS) spectrum (Figure 2f) of the applied MXene shows distinct peaks of 13.57 and 8.9 eV, and the work function was calculated to be 4.62 eV, which is similar to the literature.[14b]

Similarly, it is very necessary to make the crystal structures and luminescence properties of 2D CsPbBr$_3$ clear for the deep understanding of its well-matched work function mechanism with the novel MXene electrodes. As shown in **Figure 3**a, the SEM image of as-applied CsPbBr$_3$ nanosheets exhibit a uniformly rectangular shape with an average size of about 1.5 μm. Additionally, the slight wrinkle of 2D CsPbBr$_3$ are obviously observed from TEM image (Figure 3b), indirectly revealing its ultrathin feature and excellent flexibility. Further, its high-resolution TEM (HRTEM) image evidently demonstrates the well-resolved lattice fringe of 0.581 nm which agrees well with the lattice of cubic phase of CsPbBr$_3$ (No. 18-0364) (Figure 3c). The corresponding selected area electron diffraction (SAED) pattern displayed in inset further confirms the single crystallinity of as-prepared CsPbBr$_3$ nanosheets. Theoretically, the good crystallinity of semiconductor materials contributes to the transition of electron–hole pairs due to the inexistent defect resistance of grain
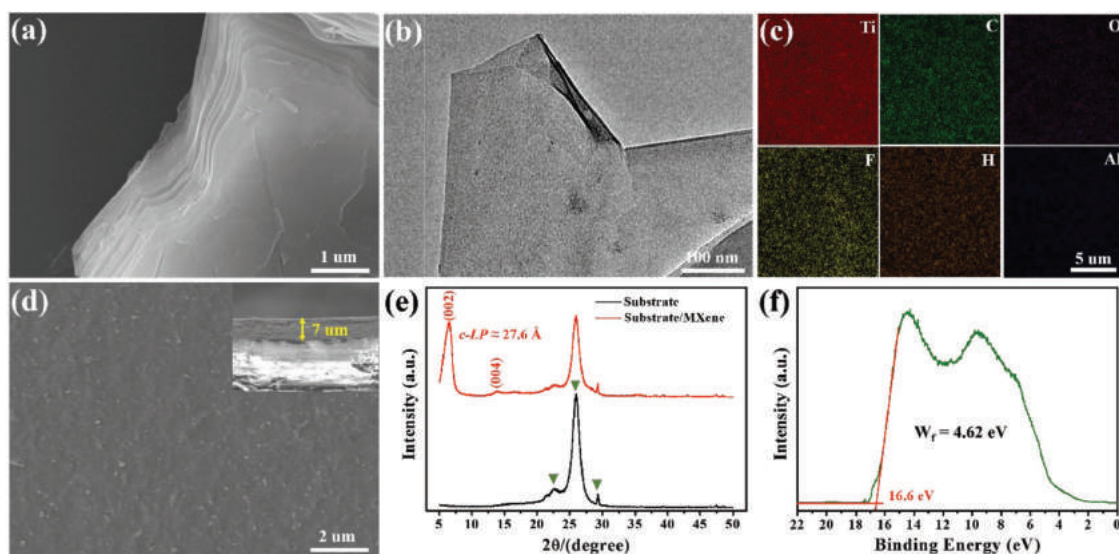
Figure 2. Morphology and structure characterization of the as-sprayed MXene. a) SEM, b) TEM, and c) EDS-mapping of the etched MXene. d) Representative SEM and the cross section of MXene electrode with 20 mL MXene solution sprayed on the substrate with an area of 12 cm × 8 cm. e) XRD of clean substrate and MXene coated electrode. f) UPS spectrum of the applied MXene.
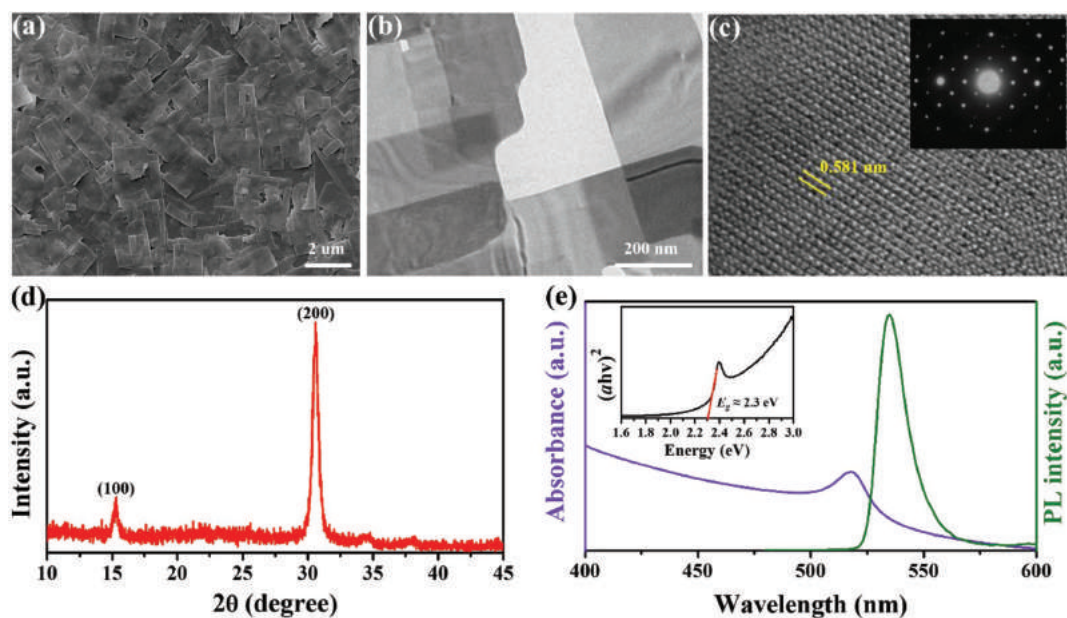
Figure 3. Characterization of as-prepared $CsPbBr_3$ nanosheets. a) SEM, b) TEM, and c) HRTEM image of the applied 2D $CsPbBr_3$. The inset of (c) is its SAED pattern. d) Representative XRD and e) UV absorption spectrum and PL spectrum of as-prepared $CsPbBr_3$ nanosheets.

boundary.[18] Furthermore, combined with the XRD of the 2D $CsPbBr_3$ (Figure 3d), two keen-edged peaks assigned to (100) and (200) planes obviously implies the single crystal characteristic and high crystallization quality.[3] Additionally, Figure 3e presents UV absorption and photoluminescence (PL) spectrum of the 2D $CsPbBr_3$. Significantly, the bright emission peak of the 2D $CsPbBr_3$ is located at 527 nm and the narrow PL spectrum with a full width at half maximum of ≈14 nm suggests a high color purity. The bandgap of as-synthesized $CsPbBr_3$ is calculated about 2.3 eV which is consistent with the previous reports.[3,11,19]

In order to further study the optoelectronic performance of the device, we investigated the optoelectronic conversion performance of single PD based on MXene electrode with 2 cm for length and 0.4 cm for width. **Figure 4**a clearly presents the *I–V* curves of as-prepared devices in dark and illumination with 405 nm light at different intensity from 0.176 to 0.53 mW mm^{-2}. The photocurrent gradually increases with the enhancement of light intensity; however, their relationship curves mostly present a nonlinear and asymmetrical behavior, evidently revealing the formation of Schottky contact resulted from the barrier of MXene/perovskite interface and surface states, such as surface defects, vacancies, and adsorption.[20] In Figure 4b, the *I–V* curves under 450 nm illumination with 7.07 mW mm^{-2} demonstrate that the dark current of the flexible PD is as low as 1 nA, and its on/off ratio is as high as 2.3×10^3 under at the same bias of 10 V. Further, we investigated the influence of MXene electrode thickness on optical conversion performance of as-prepared devices in detail. Figure S2a in the Supporting Information shows the morphology of sprayed MXene electrodes with different volume 3, 5, 10, 15, 20, and 25 mL, corresponding to the thickness of 1, 1.7, 3.5, 5.2, 7, and 8.7 µm, respectively. Obviously, with the increase of MXene thickness, the square resistance of the electrode decreases gradually (Figure S2b, Supporting Information). The inset presents the electrode conducts the LED lamp, which confirms the excellent electrical conductivity of sprayed MXene

electrode. Figure 4c shows the *I–t* curves of PDs with different thickness under 450 nm light illumination at a bias of 10 V. The lower photocurrent is tested regardless of the thinner or thicker electrodes. As a result, the optimal photocurrent up to ≈5.6 µA is obtained at 5.2 µm. This result should be ascribed to the following reasons: i) the higher square resistance of the thinner electrode makes photon-generated electron–hole pairs unable to separate immediately; ii) the lower surface flatness of the thicker MXene electrode will result in the more surface defects in contact interface and the higher the barrier, badly hindering the effective transmission of photogenerated electron–hole pairs; iii) while its thickness increases, the more MXene flakes overlap with each other, naturally resulting in increasing the transmission distance of electron–hole pairs, as schematically shown in Figure S3 in the Supporting Information.[20,21] Long distance transmission makes it difficult for the current detector to effectively detect the strength of photocurrent in a short time, thereby reducing its photocurrent. As expected, the *I–V* curves of as-prepared PDs in Figure S4 in the Supporting Information also prove the lower photocurrent.

In general, the photoresponse speed is closely related to the times of electrons and holes collected by the electrodes.[22] While the optical gain (*G*) is determined by the charge carrier lifetime and transition time as described by the equation

$$G = \frac{\tau_1}{\tau_2} \tag{1}$$

where τ_1 and τ_2 are the carrier lifetime and transition time, respectively. τ_1 depends on the semiconductor material itself, but τ_2 is mainly determined by the interelectrode spacing of electrode and applied bias voltage. Usually, the smaller the interelectrode spacing is, the more times of the photogenerated charge carriers are collected, effectively promoting the faster photoresponse of PDs. Experimentally, we investigated the *I–V* characteristics of PDs with different interelectrode spacing at the fixed thickness
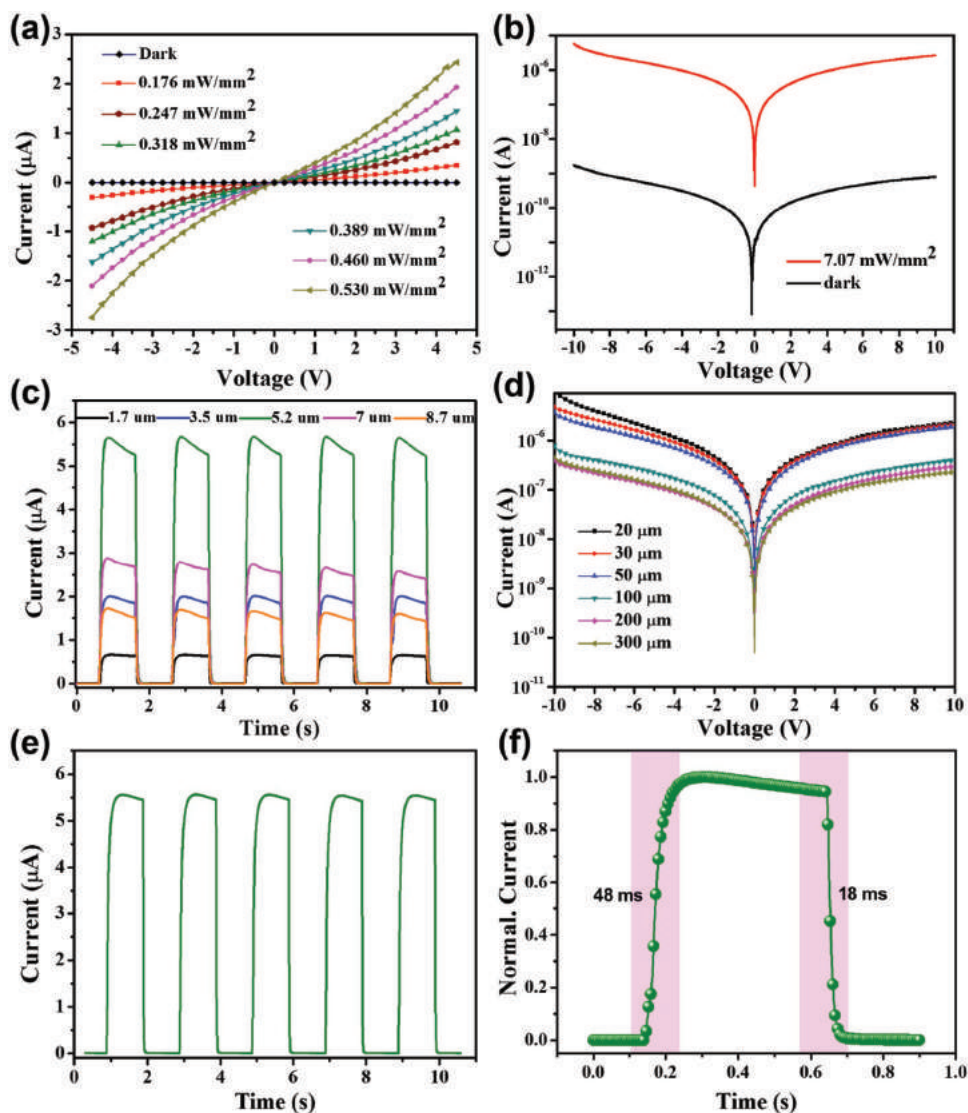
Figure 4. Characterization of the as-fabricated single PDs. a) I–V curves of as-prepared PDs in the dark and under illumination with 405 nm light at different intensity from 0.176 to 0.53 mW mm^{-2}. b) I–V curves of the PDs under the condition of illumination and dark. c) I–t curves and d) I–V curves of at various thickness of MXene and electrode spacing, respectively. e) I–t curves of as-prepared PDs with optimum condition. f) Normalized high-resolution photoresponse for rise and decay times. Above characterizations (b)–(f) are obtained under a 450 nm illumination source with 7.07 mW mm^{-2} at a bias voltage of 10 V.

of 5.2 µm (Figure S5, Supporting Information). As expected, its corresponding photocurrent indeed increases gradually with the decrease of interelectrode spacing from 300 to 20 µm (Figure 4d). Based on the above-mentioned factors, we have developed a PD with the optimal thickness and interelectrode spacing. Its photocurrent sharply rises to ≈5.7 µA under a bias of 10 V and light intensity of 7.07 mW mm^{-2} (Figure 4e). Once turning off the light, its current instantly falls to ≈1 nA, which evidently implies the fast photoresponse of as-prepared PD. Furthermore, as shown in Figure 4f, its sensitive rise/decay time was measured to be 48/18 ms, which are mostly lower than those of the previously reported PDs with metals or ITO as the electrodes. Such sensitive photoresponse is mainly ascribed to the synergistic effect of both the superior conductivity of MXene electrode, the excellent crystal quality of CsPbBr$_3$ nanosheets, and their well-matched energy level toward the fast separation and efficient extraction of

photogenerated carriers.[23] In order to indicate the photocurrent flowing in a detector divided by incident optical power, responsivity (R) can be calculated by the following formulas

$$R = \frac{I_{ph}}{PS} \tag{2}$$

where I_{ph} is the photocurrent, P is the power density, and S is the effective illumination area. The responsivity of 44.9 mA W^{-1} obtained at the light source of 450 nm is about order of magnitude higher than that of some previous reports. Moreover, detectivity (D*) reflects the photodetector's sensitivity using the following equation

$$D* = \frac{R}{\left(2qJ_{dark}\right)^{1/2}} \tag{3}$$

ADVANCED
SCIENCE NEWS
www.advancedsciencenews.com

ADVANCED
OPTICAL
MATERIALS
www.advopticalmat.de

Table 1. Performance comparisons of pervoskite PDs based on MXene and other materials as the electrode.

Active materials	Electrode materials	On/off ratio	τ_R/τ_D [ms]	Electric field [V μm^{-1}]	Reference
MAPbI$_3$	Pencil-graphite	32	<10	0.0025	[24]
MAPbI$_3$	ITO	324	100/100	0.533	[28]
MAPbBr$_3$	ITO	62	120/86	5.0	[30]
MAPbI$_3$ network	Au	340	0.3/0.4	0.05	[2b]
MAPbCl$_3$ single crystal	Au-Ti/Pt	>10^3	24/62	0.043	[31]
MAPbI$_3$/ZnO nanorods	Au/FTO	–	700/600	0.5	[25]
CsPb(Br/I)$_3$ nanorods	Au	2×10^3	680/660	4.0	[32]
CsPbI$_3$ nanoarrays	Au/ITO	–	292/234	4.2	[33]
CsPbBr$_3$ nanosheets	Pencil-graphite	10^3	0.25/0.45	0.09	[22]
CsPbBr$_3$ nanosheets	Au/ITO	>10^3	0.019/0.025	0.5	[11]
CsPbBr$_3$ nanosheets	MXene	2.3×10^3	48/18	0.2	This work

where q is the absolute value of electron charge and J_{dark} is the dark current density. According to formula (3), we can obtain the $D^* = 6.4 \times 10^8$ Jones, which further demonstrates the excellent performance of our CsPbBr$_3$/MXene-based PDs.

In addition, we compared some of the previously reported PDs with ours in on/off ratio and response time, as shown in **Table 1**. Obviously, the PDs based on MXene electrode and 2D CsPbBr$_3$ exhibit an enhancement of three orders of magnitude in on/off ratio than the PDs based on CH$_3$NH$_2$PbI$_3$ and pencil-graphite reported by Fang et al.[24] Meanwhile, the response time is about 14-fold than that of Yu's.[25] The comparable or even higher performance of as-prepared PDs attributes to the well-matched energy levels, excellent conductivity of MXene, and the excellent crystal quality of CsPbBr$_3$ nanosheets. However, the overall performance of the device is still lower than that reported by Song et al.,[11] indicating that the performance of our PDs still needs to be further improved.

The transfer mechanism of electron–hole pairs in the PDs based on MXene electrode in our work is given in **Figure 5**. When there is no illumination and bias voltage applied on as-prepared
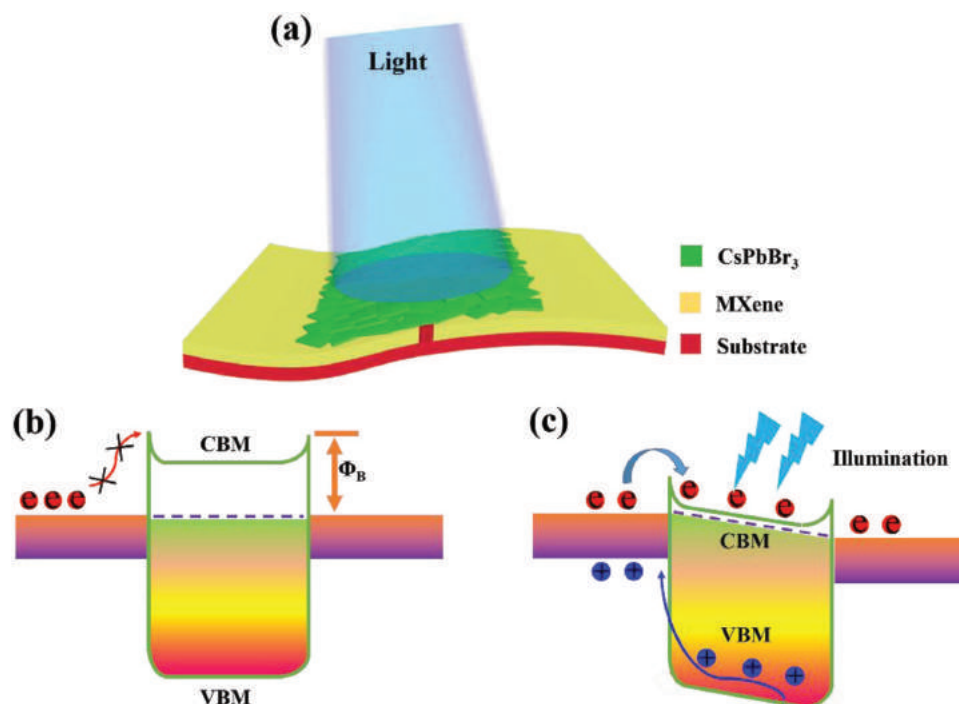
Figure 5. Transfer mechanism of photogenerated electrons and holes in dark and under illumination. a) Schematic of the single photodetector based on MXene electrode. b) Schematic diagram of the device's energy level under no illumination. Φ_B is the Schottky barrier height. CBM and VBM are the conduction band energy and valence band energy, respectively. c) Under light illumination, photon-generated electron–hole pairs migrate from CBM and VBM of CsPbBr$_3$ nanosheets to the MXene electrodes to form the photocurrent.
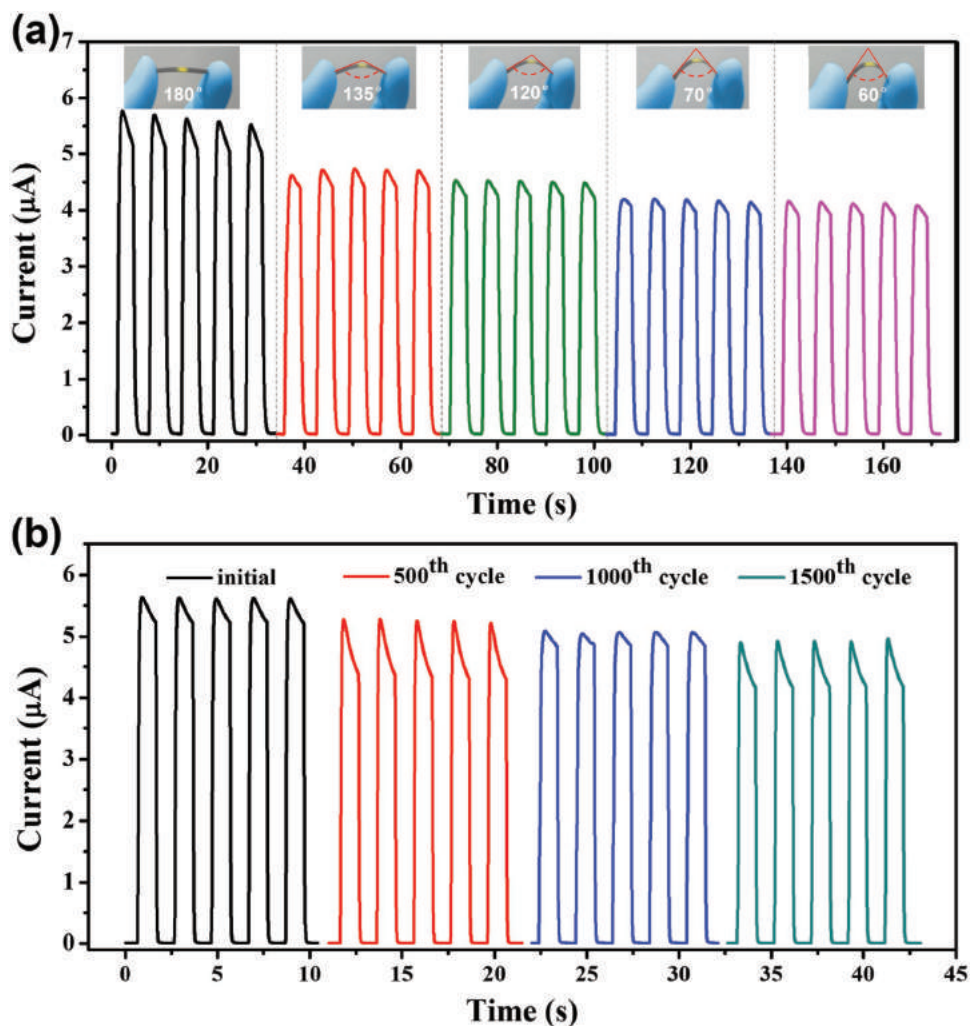
Figure 6. Flexibility and stability measurement of the as-prepared PDs. a) *I–t* curves of the PDs under the different bending angle. b) Photocurrent of as-prepared PDs after 0 bending cycles, 500 bending cycles, 1000 bending cycles, and 1500 bending cycles.

PDs, the energy level potential barrier (Schottky barrier) formed at the contact surface of MXene and CsPbBr$_3$ traps the electrons in the material and cannot allow them to be transported effectively. At the moment, the whole device is in equilibrium state. However, once the illumination energy is larger than that of the semiconductor bandgap E_g, a large number of photogenerated electron–hole pairs in CsPbBr$_3$ nanosheets are separated rapidly and have a low rate of recombination under the driving force of the reversely local electric field, which leads to the increase of free carrier concentration.[26] The high carrier concentration reduces the transmission potential barrier of electrons and significantly increases the conductivity of CsPbBr$_3$, thus showing the high photoresponse.[27] On the other hand, during the charge transfers at the interface of CsPbBr$_3$ and MXene, the accumulation of space charge and band bending in the contact region will cause the formation of depletion layer.[28] The depletion layer further assists in the improved separation of the photogenerated excitons.[29] Resultantly, under the effect of the applied electric field, the electron–hole pairs can be smoothly transported. Nevertheless, once the illumination is turned off, the carrier density decreases rapidly, resulting in the formation of Schottky barrier again.

For the flexible PDs, the external stresses releasing ability is the important criterion to evaluate its flexibility.[2a] The photoelectric properties of the MXene-based PDs at various bending curvatures are shown in **Figure 6**a. With the gradual increase of bending angle, the photocurrent decreases slightly at first and then keeps a stable state, obviously indicating the superior stress release ability of these PDs due to the excellent laminated structure of both MXene and CsPbBr$_3$ nanosheets. Further, as shown in Figure S6 in the Supporting Information, after about three months storage in atmospheric environment, the performance of the as-prepared PDs shows excellent stability and only 20% decay of the photocurrent, benefiting from the high stability of CsPbBr$_3$. The decrease in performance may be due to the fact that MXene absorbs moisture from the air, leading to the decrease of electrical conductivity. In addition, the photocurrent stability of the devices was further measured when bending at 160°. As shown in Figure 6b and S6 in the Supporting Information, compared to the initial state of as-prepared devices, the dark current almost remains unchanged and the photocurrent still retains 85% of its initial properties after bending 1500 cycles, evidently presenting the remarkable stability of as-prepared PDs.

ADVANCED
SCIENCE NEWS
www.advancedsciencenews.com

ADVANCED
OPTICAL
MATERIALS
www.advopticalmat.de

In summary, we successfully prepared the large-area and flexible PDs arrays by an easy-processable and all-sprayed-processable method. Benefiting from synergistic effect of the superior conductivity of MXene electrode, single crystal feature of 2D $CsPbBr_3$, and their well-matched energy level, the fast separation and efficient extraction of photogenerated carriers contribute to the fast photoresponse speed of 18 ms and the excellent on/off ratio of 2.3×10^3, which are comparable to the perovskite PDs with metal electrodes. In addition, the excellent flexibility and photostability are confirmed by cyclic bending tests. Importantly, by large-area arrays of the as-prepared PDs with 1665 pixel in 72 cm^2 ($\approx$24 units cm^{-2}), we successfully realized the photocommunication function. This work highlights an economic preparation method of PDs and provides potential promising applications to realize wearable electronic devices and photocommunication.

3. Experimental Section

Preparation of MXene Solution: The conductive MXene were synthesized according to our previously reported work.[15a] Typically, (76 mmol) LiF was dissolved in (30 mL 6 M) HCl solution with continuous stirring for 10 min. After completely dissolved, (1.2 g) Ti_3AlC_2 powder was added to the mixture solution, followed by stirring at 45 °C for 40 h to etch Al element. And then, the suspension was transferred to centrifuge tube to centrifuge and then washed several times with deionized (DI) water until the pH of the solution was around 6. Each wash process was performed by hand shaking and centrifuging at 3000 rpm for 5 min. The precipitate was dried at 40 °C for 24 h in vacuum. For the conductive MXene colloidal solution, (0.2 g) MXene powder was dispersed in 25 mL DI water and dealt with ultrasonic for 1 h. Finally, the obtained MXene solution was centrifuged at 3500 rpm for 45 min. The supernate was collected for further spray-coating.

Preparation of $CsPbBr_3$ Nanosheet: All the chemicals were purchased from Aladdin and used without further purification. The preparation process was referred to the previous literature.[6a,22] Briefly, (2 mmol) CsBr and (1 mmol) $PbBr_2$ were dissolved in 14 mL dimethyl sulfoxide as precursor. (2 g) Octadecaylamine was added in (10 mL) CH_3COOH (HAc) as ligands solution. (0.15 mL) Precursor was added in 1 mL ligands solution under magnetic stirring for 15 min. After uniformly mixed, (15 mL) toluene was added into the solution and stirred for another 20 min. Then, the precipitates were washed twice with toluene, and centrifuged with 5000 rpm for 2 min. Finally, the as-prepared $CsPbBr_3$ nanosheet was dispersed in (4 mL) of toluene for further characterizations, which was sonicated for 10 min before use.

Device Fabrication and Measurements: The common paper was selected as the substrate. Different amounts of MXene were sprayed on it with 96 cm^2 and treated simultaneously with infrared heating. Then, the MXene coated paper was dried at 40 °C for 1 h in vacuum. The obtained MXene conductive layers were incised by UV cold working process technique. The as-prepared 2D $CsPbBr_3$ nanosheets were also spray casted on the channel of MXene electrodes and dried at 80 °C for 5 min by hot plate. The on/off cycling performances and response speed were measured by SR570 under a pulse laser (450 nm), which was controlled by different pulse width equipped with oscilloscope (RIGOLGL1022). Keithley 2400 was used for supporting power for the detector. The *I–V* relationship was measured with Keithley 4200 and a manual probe station.

Materials Characterizations: The crystal structural characterization and phase identification of the samples were carried out by the *X* Pert Pro (Holland) *X*-ray diffract meter with Cu $K_{\alpha1}$ radiation ($\lambda = 0.154$ nm) from 5° to 90°. Surface morphology and compositions of the MXene and $CsPbBr_3$ were investigated by SEM (FEI QUANTA FEG 250, American)

and energy-dispersive X-ray spectroscopy (S4800), respectively. UPS (Escalab 250Xi, He1) and four-probe technique (RTS8, China) were applied to characterization MXene electrodes. The crystallography, UV–vis absorption spectra and photoluminescence spectra of $CsPbBr_3$ nanosheets were examined by TEM (JEOL JEM-2100, Japan) with an accelerating voltage of 200 kV, spectrophotometer (HITACHI, U-3900H, Japan) and FLS 980 (Edinburgh Instruments) spectrometer with a 450 W Xenon lamp at room temperature, respectively.

Supporting Information

Supporting Information is available from the Wiley Online Library or from the author.

Acknowledgements

Conflict of Interest

The authors declare no conflict of interest.

Keywords

[1] a) F. Teng, K. Hu, W. Ouyang, X. Fang, *Adv. Mater.* **2018**, *30*, 1706262; b) H. Wang, D. H. Kim, *Chem. Soc. Rev.* **2017**, *46*, 5204; c) Z. Zheng, L. Gan, J. Zhang, F. Zhuge, T. Zhai, *Adv. Sci.* **2017**, *4*, 1600316.

[2] a) C. Xie, F. Yan, *Small* **2017**, *13*, 1701822; b) H. Deng, X. Yang, D. Dong, B. Li, D. Yang, S. Yuan, K. Qiao, Y. B. Cheng, J. Tang, H. Song, *Nano Lett.* **2015**, *15*, 7963.

[3] X. Liu, D. Yu, F. Cao, X. Li, J. Ji, J. Chen, X. Song, H. Zeng, *Small* **2017**, *13*, 1700364.

[4] M. Hossain, G. S. Kumar, S. N. Barimar Prabhava, E. D. Sheerin, D. McCloskey, S. Acharya, K. D. M. Rao, J. J. Boland, *ACS Nano* **2018**, *12*, 4727.

[5] a) S. I. Park, J. H. Ahn, X. Feng, S. Wang, Y. Huang, J. A. Rogers, *Adv. Funct. Mater.* **2008**, *18*, 2673; b) Y. Y. Peng, B. Akuzum, N. Kurra, M. Q. Zhao, M. Alhabeb, B. Anasori, E. C. Kumbur, H. N. Alshareef, M. D. Ger, Y. Gogotsi, *Energy Environ. Sci.* **2016**, *9*, 2847.

[6] a) X. Li, D. Yu, J. Chen, Y. Wang, F. Cao, Y. Wei, Y. Wu, L. Wang, Y. Zhu, Z. Sun, J. Ji, Y. Shen, H. Sun, H. Zeng, *ACS Nano* **2017**, *11*, 2015; b) T. Yang, Y. Zheng, Z. Du, W. Liu, Z. Yang, F. Gao, L. Wang, K. C. Chou, X. Hou, W. Yang, *ACS Nano* **2018**, *12*, 1611;

**ADVANCED
SCIENCE NEWS**

www.advancedsciencenews.com

**ADVANCED
OPTICAL
MATERIALS**

www.advopticalmat.de

c) G. R. Yettapu, D. Talukdar, S. Sarkar, A. Swarnkar, A. Nag, P. Ghosh, P. Mandal, *Nano Lett.* **2016**, *16*, 4838.

[7] a) Z. Gu, Z. Huang, C. Li, M. Li, Y. Song, *Sci. Adv.* **2018**, *4*, eaat2390; b) Q. A. Akkerman, G. Rainò, M. V. Kovalenko, L. Manna, *Nat. Mater.* **2018**, *17*, 394.

[8] T. Zhang, J. Wu, P. Zhang, W. Ahmad, Y. Wang, M. Alqahtani, H. Chen, C. Gao, Z. D. Chen, Z. Wang, S. Li, *Adv. Opt. Mater.* **2018**, *6*, 1701341.

[9] N. Yantara, S. Bhaumik, F. Yan, D. Sabba, H. A. Dewi, N. Mathews, P. P. Boix, H. V. Demir, S. Mhaisalkar, *J. Phys. Chem. Lett.* **2015**, *6*, 4360.

[10] L. Lv, Y. Xu, H. Fang, W. Luo, F. Xu, L. Liu, B. Wang, X. Zhang, D. Yang, W. Hu, A. Dong, *Nanoscale* **2016**, *8*, 13589.

[11] J. Z. Song, L. Xu, J. Li, J. Xue, Y. Dong, X. Li, H. B. Zeng, *Adv. Mater.* **2016**, *28*, 4861.

[12] J. Yang, C. Bao, K. Zhu, T. Yu, Q. Xu, *ACS Appl. Mater. Interfaces* **2018**, *10*, 1996.

[13] a) S. Lai, S. K. Jang, J. H. Cho, S. Lee, *Nanoscale* **2018**, *10*, 5191; b) J. Xu, J. Shim, J. H. Park, S. Lee, *Adv. Funct. Mater.* **2016**, *26*, 5328.

[14] a) Z. Kang, Y. Ma, X. Tan, M. Zhu, Z. Zheng, N. Liu, L. Li, Z. Zou, X. Jiang, T. Zhai, Y. Gao, *Adv. Electron. Mater.* **2017**, *3*, 1700165; b) Z. Wang, H. Kim, H. N. Alshareef, *Adv. Mater.* **2018**, *30*, 1706656.

[15] a) H. C. Huang, H. Su, H. T. Zhang, L. D. Xu, X. Chu, C. F. Hu, H. Liu, N. J. Chen, F. Y. Liu, W. Deng, B. N. Gu, H. P. Zhang, W. Q. Yang, *Adv. Electron. Mater.* **2018**, *4*, 1800179; b) K. Hantanasirisakul, M. Q. Zhao, P. Urbankowski, J. Halim, B. Anasori, S. Kota, C. E. Ren, M. W. Barsoum, Y. Gogotsi, *Adv. Electron. Mater.* **2016**, *2*, 1600050; c) R. Sun, H. B. Zhang, J. Liu, X. Xie, R. Yang, Y. Li, S. Hong, Z. Z. Yu, *Adv. Funct. Mater.* **2017**, *27*, 1702807.

[16] a) M. Q. Zhao, X. Xie, C. E. Ren, T. Makaryan, B. Anasori, G. Wang, Y. Gogotsi, *Adv. Mater.* **2017**, *29*, 1702410; b) M. Naguib, M. Kurtoglu, V. Presser, J. Lu, J. Niu, M. Heon, L. Hultman, Y. Gogotsi, M. W. Barsoum, *Adv. Mater.* **2011**, *23*, 4248; c) E. Pomerantseva, Y. Gogotsi, *Nat. Energy* **2017**, *2*, 17089.

[17] N. Kurra, B. Ahmed, Y. Gogotsi, H. N. Alshareef, *Adv. Energy Mater.* **2016**, *6*, 1601372.

[18] a) Y. Liu, Y. Zhang, K. Zhao, Z. Yang, J. Feng, X. Zhang, K. Wang, L. Meng, H. Ye, M. Liu, S. F. Liu, *Adv. Mater.* **2018**, *30*, 1707314; b) M. I. Saidaminov, A. L. Abdelhady, B. Murali, E. Alarousu, V. M. Burlakov, W. Peng, I. Dursun, L. Wang, Y. He, G. Maculan, A. Goriely, T. Wu, O. F. Mohammed, O. M. Bakr, *Nat. Commun.* **2015**, *6*, 7586; c) Z. Z. Chen, Y. P. Wang, Y. H. Shi, B. Hsu, Z. Yang, J. Shi, *Adv. Electron. Mater.* **2016**, *2*, 1600248.

[19] J. L. Duan, Y. Y. Zhao, B. L. He, Q. W. Tang, *Small* **2018**, *14*, 1704443.

[20] H. Kind, H. Yan, B. Messer, M. Law, P. Yang, *Adv. Mater.* **2002**, *14*, 158.

[21] Y. Xia, T. S. Mathis, M. Q. Zhao, B. Anasori, A. Dang, Z. Zhou, H. Cho, Y. Gogotsi, S. Yang, *Nature* **2018**, *557*, 409.

[22] F. Cao, D. Yu, X. Li, Y. Zhu, Z. Sun, Y. Shen, Y. Wu, Y. Wei, H. Zeng, *J. Mater. Chem. C* **2017**, *5*, 7441.

[23] L. Dou, Y. M. Yang, J. You, Z. Hong, W. H. Chang, G. Li, Y. Yang, *Nat. Commun.* **2014**, *5*, 5404.

[24] H. Fang, J. Li, J. Ding, Y. Sun, Q. Li, J. L. Sun, L. Wang, Q. Yan, *ACS Appl. Mater. Interfaces* **2017**, *9*, 10921.

[25] J. Yu, X. Chen, Y. Wang, H. Zhou, M. Xue, Y. Xu, Z. Li, C. Ye, J. Zhang, P. A. van Aken, P. D. Lund, H. Wang, *J. Mater. Chem. C* **2016**, *4*, 7302.

[26] Y. Hu, J. Zhou, P. H. Yeh, Z. Li, T. Y. Wei, Z. L. Wang, *Adv. Mater.* **2010**, *22*, 3327.

[27] a) T. Zhang, J. Wu, P. Zhang, W. Ahmad, Y. F. Wang, M. Alqahtani, *Adv. Funct. Mater.* **2018**, *28*, 1705589; b) H. Chen, C. M. Gao, Z. D. Chen, Z. M. Wang, S. B. Li, *Adv. Opt. Mater.* **2018**, *6*, 1701341.

[28] X. Hu, X. Zhang, L. Liang, J. Bao, S. Li, W. Yang, Y. Xie, *Adv. Funct. Mater.* **2014**, *24*, 7373.

[29] S. Aharon, S. Gamliel, B. El Cohen, L. Etgar, *Phys. Chem. Chem. Phys.* **2014**, *16*, 10512.

[30] S. Zhuo, J. Zhang, Y. Shi, Y. Huang, B. Zhang, *Angew. Chem., Int. Ed.* **2015**, *54*, 5693.

[31] G. Maculan, A. D. Sheikh, A. L. Abdelhady, M. I. Saidaminov, M. A. Haque, B. Murali, E. Alarousu, O. F. Mohammed, T. Wu, O. M. Bakr, *J. Phys. Chem. Lett.* **2015**, *6*, 3781.

[32] X. Tang, Z. Zu, H. Shao, W. Hu, M. Zhou, M. Deng, W. Chen, Z. Zang, T. Zhu, J. Xue, *Nanoscale* **2016**, *8*, 15158.

[33] A. Waleed, M. M. Tavakoli, L. Gu, S. Hussain, D. Zhang, S. Poddar, Z. Wang, R. Zhang, Z. Fan, *Nano Lett.* **2017**, *17*, 4951.